Available online at www.sciencedirect.com
ScienceDirect
Comput. Methods Appl. Mech. Engrg. 341 (2018) 113–132
Computer methods in applied mechanics and engineering
www.elsevier.com/locate/cma

Inversely designed micro-textures for robust Cassie–Baxter mode of super-hydrophobicity

Yongbo Deng[a,*], Dario Mager[b], Yue Bai[c], Teng Zhou[d], Zhenyu Liu[c], Liping Wen[e], Yihui Wu[a], Jan G. Korvink[b,*]

[a] *State Key Laboratory of Applied Optics, Changchun Institute of Optics, Fine Mechanics and Physics (CIOMP), Chinese Academy of Sciences, Changchun 130033, China*
[b] *Institute of Microstructure Technology (IMT), Karlsruhe Institute of Technology (KIT), Hermann-von-Helmholtzplatz 1, Eggenstein-Leopoldshafen 76344, Germany*
[c] *Changchun Institute of Optics, Fine Mechanics and Physics (CIOMP), Chinese Academy of Sciences, Changchun 130033, China*
[d] *Mechanical and Electrical Engineering College, Hainan University, Haikou, Hainan 570228, PR China*
[e] *Laboratory of Bioinspired Smart Interfacial Science, Technical Institute of Physics and Chemistry, Chinese Academy of Sciences, Beijing 100190, PR China*

Received 5 December 2017; received in revised form 2 May 2018; accepted 26 June 2018
Available online 3 July 2018

Abstract

The robust Cassie–Baxter mode of the wetting behaviour on a micro-textured solid surface, is a key topography element yielding stable super-hydrophobicity. To meet this purpose, we propose an inverse computational design procedure for the discovery of suitable periodic micro-textures, based on three different tilings of the plane. The symmetric tiles of the lattice are regular triangles, quadrangles, and hexagons. The goal of the inverse design procedure is to achieve the robust Cassie–Baxter state, in which the liquid/vapour interface is mathematically described using the Young–Laplace equation on the lattice, and a topology optimisation approach is utilised to construct a variational problem for the inverse design procedure. Based on numerical calculations of the constructed variational problem, underlying effects are revealed for several factors, including the Bond number, duty ratio, feature size, and lattice constant. The effects of feature size and lattice constant provide approaches for compromisingly considering the robustness of the Cassie–Baxter mode and manufacturability of the inversely designed micro-textures; the effect of the lattice constant permits the scaling properties of the derived patterns, and this in turn provides an approach to avoid the elasto-capillary instability driven collapse of the micro/nanostructures in the derived micro-textures. Further, a monolithic inverse design procedure for the periodic micro-textures is proposed in the conclusions, with synthetically considering the manufacturability as well as contact angle and surface-volume ratio of the liquid bulge held by the supported liquid/vapour interface.

Keywords: Micro-texture; Inverse design; Cassie–Baxter mode; Super-hydrophobicity; Topology optimisation

* Corresponding authors.
E-mail addresses: dengyb@ciomp.ac.cn (Y. Deng), jan.korvink@kit.edu (J.G. Korvink).

https://doi.org/10.1016/j.cma.2018.06.034
0045-7825/

1. Introduction

Wetting behaviour is an important aspect in surface chemistry, and the wettability of a solid surface can be categorised into hydrophobicity, hydrophilicity, oleophobicity, oleophilicity, amphiphilicity, and amphiphobicity [1]. Recent achievements in the construction of artificial surfaces for special degrees of wettability are typically focused on super-hydrophobicity, i.e., achieving a contact angle for water larger than 150° on a hydrophobic substrate [2]. Super-hydrophobicity has a variety of practical applications, e.g., constructing smart devices for anti-drag and lubrication [3], microfluidics [4], electrohydrodynamics [5], separation of oil and water [6,7], and self-cleaning coatings [8], to name the most typical.

In the previous reports, two approaches have been commonly used to design artificial surfaces with super-hydrophobicity, i.e., chemically modifying the surfaces using materials with low surface free energy, or creating micro-textures on hydrophobic surfaces [9]. Materials with low surface free energy, e.g., vinyl alcohol [10,11], alkylpyrrole [12], polystyrene [13], and edible materials [14] to name the most important, have been utilised to fabricate an artificial surface. The micro-textures have been augmented by periodic circular posts, square posts, tapered cones, dual-scale micro-structures, and spontaneous wrinkling, to form the artificial roughness [15–21]. Inspired by super-hydrophobicity in nature, a variety of concepts including lotus leaves, water-strider legs, and textiles, and bio-inspired micro-textures, have been discussed in [9,22–28], and have been utilised for liquid–solid adhesion [29]. The theory, design, and applications for such bio-inspired micro-textures have been summarised in [30]. The function of the micro-textures on a solid surface is to decrease the equivalent surface free energy by increasing the surface roughness, because the wettability of the solid surface is commonly determined by its microscopical morphology and the surface free energy of its material [1]. For a given substrate, the wetting behaviour is dominated by its micro-textures. Most of the currently utilised morphologies of micro-textures for super-hydrophobic surfaces are either bio-inspired or structured using posts with regular cross-sections. This paper introduces a novel and efficient mathematical-approach to determine the reasonable micro-textures for super-hydrophobic surfaces, where the patterns of the micro-textures are inversely designed based on numerical computation instead of bio-inspiration and physical intuition. The inverse design procedure is implemented by a topology optimisation approach.

Topology optimisation is a full-parameter method used to inversely determine the geometrical configurations of structures [31]. In contrast to designing devices by tuning a handful of structural parameters, this approach utilises the full parameter space to design structures solely based on the user's desired performance specification. Therefore, it can inversely find both a reasonable shape and topology. Simultaneously, it is a more general computational design method than shape optimisation, which usually improves the performance of a device by adjusting the structural boundaries and maintaining the topology of the structure without change. On the other hand, topology optimisation approach can ensure the manufacturability of a structure by controlling its feature size [32]. Currently, topology optimisation has been applied to multiple physical problems, e.g. acoustics, electromagnetics, fluidic dynamics, optics, thermodynamics, and multidisciplinary/interdisciplinary design problems of structures and materials [33–50]. It is therefore a natural choice methodology for the current task.

On a solid surface with micro-textures, the surface roughness factor induced by the micro-textures should be included in the evaluation of its wettability. For a flat surface, its wettability is determined by the surface free energy of the solid as the Young mode sketched for a droplet in Fig. 1a [51]. For a rough surface with micro-textures, two different wetting modes can exist, i.e., the Wenzel and Cassie–Baxter modes (Fig. 1b and c) [52,53]. In the Wenzel mode (Fig. 1b), the liquid completely fills the micro-textures on the rough surface. The Young mode is correlated with the surface roughness factor, where the hydrophobicity of the rough surface increases along with the increase of the surface roughness. In the Cassie–Baxter mode, vapour pockets are trapped in the micro-textures (Fig. 1c), so that the rough surface is equivalent to a composite surface of solid and vapour. The Young mode is correlated with the chemical heterogeneity of the rough surface, and surface roughness also increases the hydrophobicity of the solid surface.

For a rough surface, the wetting mode can change from the Cassie–Baxter case to the Wenzel case, when the liquid is physically pressed [54,55]. In this mode transition process, the liquid fills the micro-textures on the rough surface with a decrease in hydrophobicity. In the Cassie–Baxter mode, the vapour pockets result in the existence of the liquid/vapour interface, which is supported by the micro-textures (Fig. 2). Under the effect of contact angle hysteresis [56], the three-phase contact lines of the liquid/vapour interface can be anchored at the geometrically singular corners formed by the top and side walls of the micro-textures. If the difference between the static pressure inside and outside the liquid is large enough to make the contact angle between the liquid/vapour interface and side

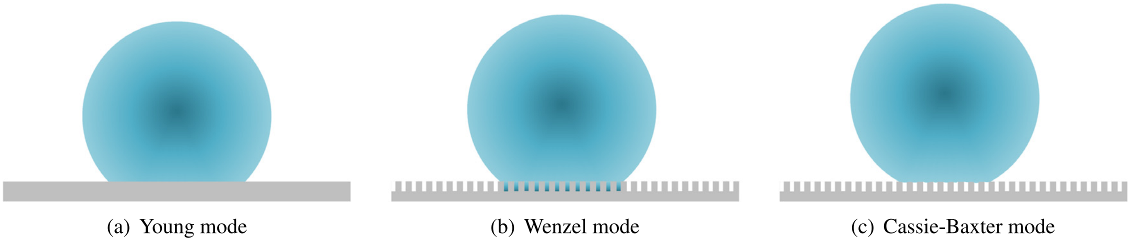

Fig. 1. Sketched modes of the wetting behaviour of a droplet on the flat and rough surfaces: (a) Young mode; (b) Wenzel mode; (c) Cassie–Baxter mode.

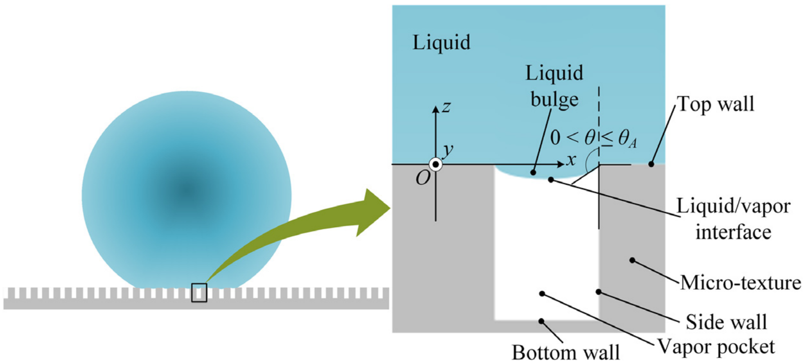

Fig. 2. Sketched liquid/vapour interface supported by the micro-textures, where θ is the contact angle at the geometrically singular corners between the top and side walls of the micro-textures, θ_A is the critical advancing value of the contact angle, and the duty ratio of the micro-textures is the ratio of the top-wall area to the sum area of the top and bottom walls. A coordinate system is sketched with z representing the vertical coordinate of the liquid/vapour interface and xOy plane localised on the top wall of one unit cell of the micro-textures, where the origin O is at the top-centre of the unit cell, x and y are respectively the abscissa and ordinate of the liquid/vapour interface.

wall of the micro-textures reach its critical advancing value, the liquid/vapour interface will burst and transition will occur from the Cassie–Baxter mode to the Wenzel mode. As the contact angle evolves towards its critical advancing value, the robustness of the Cassie–Baxter mode will be weakened; simultaneously, the liquid/vapour interface supported by the micro-textures will become more convex, and the volume of the liquid bulge held by the liquid/vapour interface will become larger. Therefore, reasonable micro-textures on a rough surface can keep the Cassie–Baxter mode from transition, enhance the stability of super-hydrophobicity by reducing the convexity of the liquid/vapour interface, and by keeping the contact angle aloof of its crucial advancing value.

Based on the above introduction, this paper focuses on the topology optimisation-based inverse design of micro-textures for super-hydrophobicity in the Cassie–Baxter mode, where the design goal is to optimise the robustness measurement of the Cassie–Baxter mode and this measurement is equivalently defined to be the convexity of the liquid/vapour interface supported by the micro-textures. Such design goal is of more physical implication than controlling the contact angle of a wetting behaviour in the Cassie–Baxter mode, because the microscopical liquid/vapour interface plays the dominant role of determining the contact angle that is one macroscopical performance of it supported by the micro-textures. In Section 2, the inverse design model and the corresponding analysis and solution methods are introduced for periodic micro-textures with regular triangle, quadrangle, and hexagon lattices. In Section 3, the patterns for the micro-textures are inversely designed and analysed under consideration of the effects of various factors, including the surface tension of the liquid, and the duty ratio, feature size and lattice constant of the micro-textures, where the duty ratio is the ratio of the top-wall area to the sum area of the top and bottom walls of the micro-textures (Fig. 2). Further, the paper is concluded in Section 4, where a monolithic inverse design procedure is proposed by including the synthetical consideration of the manufacturability of the micro-textures, contact angle of the liquid, and surface-volume ratio of the liquid bulge held by the liquid/vapour interface.

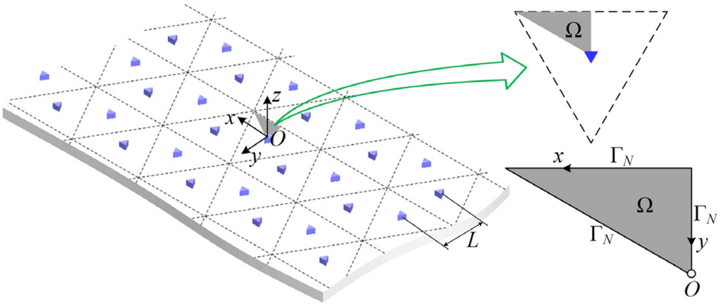

(a) Periodicity with regular triangle

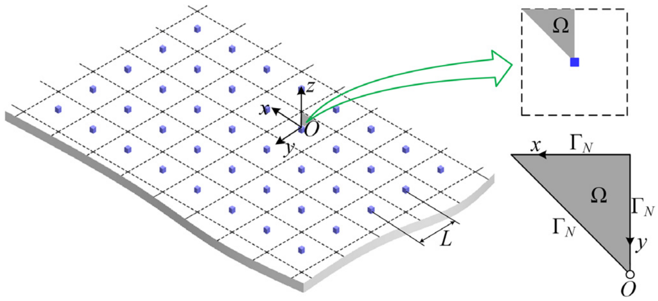

(b) Periodicity with regular quadrangle

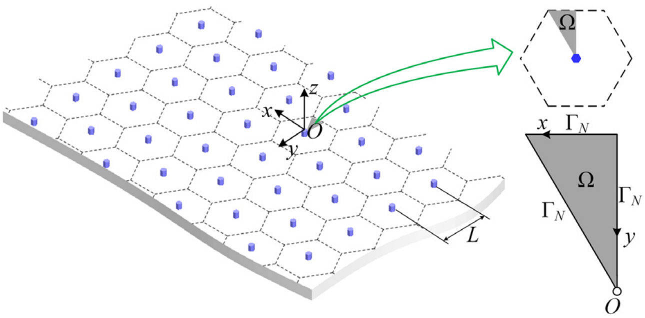

(c) Periodicity with regular hexagon

Fig. 3. Sketches for micro-textures with triangular, quadrangular, and hexagonal periodicity. x, y and z are the abscissa, ordinate, and vertical coordinates of the liquid/vapour interface supported by one lattice of the periodic micro-textures; O is origin of the coordinate system and it localises at the top-centre of the lattice; Ω is the irreducible triangle corresponding to a lattice; Γ_N denotes a symmetry boundary of the irreducible triangle.

2. Method

For a fixed static pressure difference, the suitability of micro-textures for super-hydrophobicity can be measured by the robustness of the Cassie–Baxter mode. Therefore, the micro-textures on a solid surface are inversely designed by optimising the robustness of the Cassie–Baxter mode.

2.1. Modelling

The roughness of a solid surface usually features some form of spacial periodicity [57]. Therefore, micro-textures for super-hydrophobicity are modelled with spacial periodicity in the following. There are three types of lattices (i.e. regular triangle, quadrangle and hexagon unit cells) that can fully cover the solid surface (Fig. 3). As demonstrated in Fig. 3, each of the lattice cells can be reduced into a irreducible triangle, based on its symmetry. The patterns of

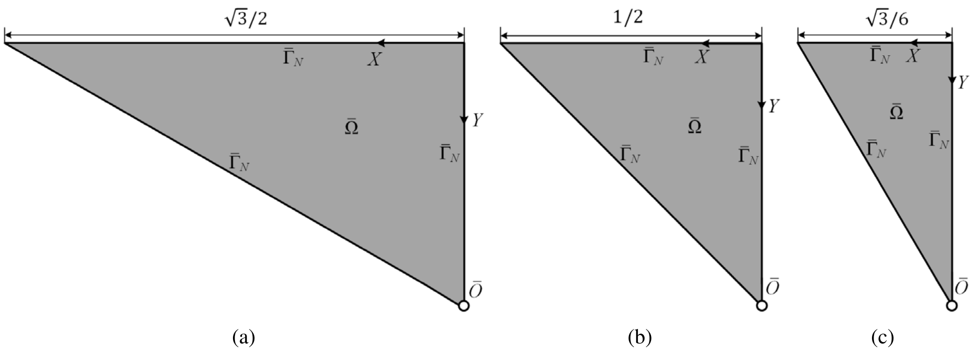

Fig. 4. Dimensionless counterparts of the irreducible triangles corresponding to the regular triangle, quadrangle, and hexagonal lattices.

the micro-textures on the solid surface can therefore be inversely designed for each irreducible triangle; the periodic micro-textures of a primitive cell is then formed by reflections along the symmetry axes, followed by an extruding operation. Under equilibrium, the liquid/vapour interface supported by periodic micro-textures is a two-dimensional (2D) manifold with constant Riemann curvature, which can be described by the Young–Laplace equation defined on one of the irreducible triangles [58,59]:

$$\begin{aligned}
&\nabla_{\mathbf{x}} \cdot \left(\sigma \frac{\nabla_{\mathbf{x}} z}{\sqrt{1 + |\nabla_{\mathbf{x}} z|^2}} \right) = P_0, \text{ in } \varOmega, \\
&\sigma \frac{\nabla_{\mathbf{x}} z}{\sqrt{1 + |\nabla_{\mathbf{x}} z|^2}} \cdot \mathbf{n} = 0, \text{ on } \varGamma_N, \\
&z = 0, \text{ at } O,
\end{aligned} \tag{1}$$

where σ is the surface tension; P_0 is the difference between the static pressure inside and outside the liquid; z is the vertical coordinate of the point on the liquid/vapour interface; $\mathbf{x} = (x, y)$ is the abscissa and ordinate of a point on the liquid/vapour interface; $\nabla_{\mathbf{x}} = \left(\frac{\partial}{\partial x}, \frac{\partial}{\partial y} \right)$ is the gradient operation defined on the xOy plane, with O representing the coordinate origin; $\varOmega$ is one of the irreducible triangles shown in Fig. 3; $\varGamma_N$ is a symmetry boundary, because the periodicity of the micro-textures is achieved based on the symmetrising operation of the micro-textures in an irreducible triangle; $\mathbf{n}$ is the outward unit normal on $\partial\varOmega$. To ensure uniqueness of the solution, the liquid/vapour interface is fixed at the symmetry centre of the lattices, and the least constraint introduced for Eq. (1) defined on the lattices shown in Fig. 3. The dimensionless counterpart of Eq. (1) is

$$\begin{aligned}
&\nabla \cdot \left(Bo^{-1} \frac{\nabla \bar{z}}{\sqrt{(L/z_0)^2 + |\nabla \bar{z}|^2}} \right) = 1, \text{ in } \bar{\varOmega}, \\
&Bo^{-1} \frac{\nabla \bar{z}}{\sqrt{(L/z_0)^2 + |\nabla \bar{z}|^2}} \cdot \mathbf{n} = 0, \ on \ \bar{\varGamma}_N, \\
&\bar{z} = 0, \text{ at } \bar{O},
\end{aligned} \tag{2}$$

where $\bar{z} = z/z_0$ is the normalised vertical coordinate on the liquid/vapour interface, with z_0 representing the magnitude of z; L is the lattice constant of the spacial periodicity, and it is the centre-to-centre distance between two neighbouring lattices; $\mathbf{X} = \mathbf{x}/L = (X, Y)$ is the dimensionless coordinate; $Bo = (P_0 L)/\sigma$ is an equivalent form of the Bond number $\left(\rho g L^2\right)/\sigma$ used to evaluate the relative importance of gravity compared to a surface tension force with ρ and g respectively representing the density of the liquid and acceleration of gravity [60]; $\bar{\varOmega}$, $\bar{\varGamma}_N$, $\bar{\varGamma}_D$ and $\bar{O}$ are the dimensionless counterparts of $\varOmega$, $\varGamma_N$, $\varGamma_D$ and O, respectively (Fig. 4); $\nabla = \left(\frac{\partial}{\partial X}, \frac{\partial}{\partial Y} \right)$ is the gradient operator defined on $\bar{\varOmega}$.

Because a 2D manifold with constant Riemann curvature has uniform convexity, the volume of the liquid bulge supported by the micro-textures in an irreducible triangle can be calculated to be $z_0 L^2 \left| \int_{\bar{\varOmega}} \bar{z} \, \mathrm{d}\bar{\varOmega} \right|$. The integrals

$\left|\int_{\bar{\Omega}} \bar{z}\, \mathrm{d}\bar{\Omega}\right|$ and $\left(\int_{\bar{\Omega}} \bar{z}^2\, \mathrm{d}\bar{\Omega}\right)^{\frac{1}{2}}$ can be regarded to be two different norms of $\bar{z} \in \mathcal{H}\left(\bar{\Omega}\right)$, where $\mathcal{H}\left(\bar{\Omega}\right)$ is the first order Hilbert functional space defined on $\bar{\Omega}$. According to the equivalence of norms [61], $\left|\int_{\bar{\Omega}} \bar{z}\, \mathrm{d}\bar{\Omega}\right|^2$ is equivalent to $\int_{\bar{\Omega}} \bar{z}^2\, \mathrm{d}\bar{\Omega}$, because two constants C_1 and C_2 ($C_2 \geq C_1 > 0$) exist for the inequality $C_1 \left|\int_{\bar{\Omega}} \bar{z}\, \mathrm{d}\bar{\Omega}\right| \leq \left(\int_{\bar{\Omega}} \bar{z}^2\, \mathrm{d}\bar{\Omega}\right)^{\frac{1}{2}} \leq C_2 \left|\int_{\bar{\Omega}} \bar{z}\, \mathrm{d}\bar{\Omega}\right|$. Therefore, the well-posed integral $\int_{\bar{\Omega}} \bar{z}^2\, \mathrm{d}\bar{\Omega} / \left|\bar{\Omega}\right|$ is utilised to equivalently measure the convexity of the liquid/vapour interface, and hence it is defined to be the robustness measurement of the Cassie–Baxter mode, where $\left|\bar{\Omega}\right|$ represents the area of $\bar{\Omega}$. Because a smaller robustness measurement corresponds to a more robust Cassie–Baxter mode, the goal of inverse design is to find a micro-texture pattern corresponding to a minimum value of the robustness measurement. For the liquid/vapour interface with uniform convexity, minimising the defined robustness-measurement $\int_{\bar{\Omega}} \bar{z}^2\, \mathrm{d}\bar{\Omega} / \left|\bar{\Omega}\right|$ is equivalent to reducing its convexity and the liquid-bulge volume yet maintaining the contact angle aloof of its crucial advancing value, further ensuring the stability of the Cassie–Baxter state for the wetting behaviour on a micro-textured solid surface.

A variational problem is now constructed based on the topology optimisation approach, in which a design variable is defined on one of the irreducible triangles to represent the pattern of the micro-textures. This design variable is used to interpolate the Bond number in Eq. (2). The constructed variational problem will be iteratively solved using a numerical optimisation procedure. To ensure numerical stability, this paper smoothes the design variable using a Helmholtz filter [62], furthermore, the smoothed design variable is projected by the threshold method [63,64]; the projected design variable, nominated to be the physical density, replaces the design variable in implementing the interpolation of the Bond number as

$$Bo^{-1} = Bo_l^{-1} + \left(Bo_s^{-1} - Bo_l^{-1}\right) \frac{q\left(1-\gamma_p\right)}{q+\gamma_p}, \tag{3}$$

where γ_p is the physical density, with 0 representing the micro-textures, and 1 the blankness thereof; Bo_l is the Bond number at the liquid–vapour interface; Bo_s is the Bond number at the top wall of the micro-textures; q is a parameter used to tune the convexity of the interpolation, and it is found to be 10^{-4} based on numerical experiments. Theoretically, Bo_s should be zero to ensure the complete dominance of surface tension, which approximates a flat liquid–solid interface; numerically, it is reasonably chosen to be the small finite value $10^{-5} Bo_l$ satisfying $Bo_s \ll Bo_l$, to ensure the stability of the numerical implementation. Then, the variational problem is constructed to be

$$\text{find } 0 \leq \gamma \leq 1 \text{ to minimise } \frac{J}{J_0} \text{ with } J = \frac{1}{\left|\bar{\Omega}\right|} \int_{\bar{\Omega}} \bar{z}^2\, \mathrm{d}\bar{\Omega}, \text{ constrained by:}$$

$$\left\{\begin{array}{l} \left\{\begin{array}{ll} \nabla \cdot \left(Bo^{-1} \dfrac{\nabla \bar{z}}{\sqrt{\left(L/z_0\right)^2 + \left|\nabla \bar{z}\right|^2}}\right) = 1, \; in \; \bar{\Omega}, & \\ Bo^{-1} \dfrac{\nabla \bar{z}}{\sqrt{\left(L/z_0\right)^2 + \left|\nabla \bar{z}\right|^2}} \cdot \mathbf{n} = 0, \; on \; \bar{\Gamma}_N, & \text{(Young–Laplace equation)} \\ \bar{z} = 0, \; at \; \bar{O}, & \end{array}\right. \\ \left\{\begin{array}{ll} \nabla \cdot \left(r_f^2 \nabla \gamma_f\right) + \gamma_f = \gamma, \; in \; \bar{\Omega}, & \\ r_f^2 \nabla \gamma_f \cdot \mathbf{n} = 0, \; on \; \bar{\Gamma}_N, & \text{(Helmholtz filter)} \\ \gamma_f = 0, \; at \; \bar{O}, & \end{array}\right. \\ \gamma_p = \dfrac{\tanh\left(\beta\xi\right) + \tanh\left(\beta\left(\gamma_f - \xi\right)\right)}{\tanh\left(\beta\xi\right) + \tanh\left(\beta\left(1-\xi\right)\right)}, \quad \text{(Threshold projection)} \\ \left|f_d - f_0\right| \leq 10^{-3}, \text{ with } f_d = \dfrac{1}{\left|\bar{\Omega}\right|} \displaystyle\int_{\bar{\Omega}} 1 - \gamma_p\, \mathrm{d}\bar{\Omega}, \quad \text{(Duty-ratio constraint)} \end{array}\right. \tag{4}$$

where a duty-ratio constraint is imposed on the micro-textures, with f_d representing the duty ratio and $f_0 \in (0, 1)$ the specified duty ratio with a permitted tolerance 10^{-3}; J_0 is the robustness-measurement value corresponding to the periodic triangle, quadrangle or hexagon posts with a specified duty ratio f_0; γ is the design variable; γ_f is the filtered design variable; r_f is the radius of the Helmholtz filter; β and $\xi \in (0, 1)$ are the projection parameters with values chosen based on numerical experiments [64]. Especially, r_f can be used to control the feature size of the micro-textures. By numerically solving the variational problem in Eq. (4), patterns of micro-textures can be inversely designed in the irreducible triangles.

2.2. Analysing and solving

To solve the variational problem in Eq. (4), a gradient-based iterative procedure can be used, for which the gradient of the robustness measurement and duty ratio can be determined by a Lagrangian multiplier-based adjoint method [65]. Based on the adjoint method, the gradient of the robustness measurement yields

$$\frac{\delta J}{J_0} = \frac{1}{J_0} \int_{\bar{\Omega}} -\gamma_{fa} \delta\gamma \, \mathrm{d}\bar{\Omega}, \tag{5}$$

where δJ and $\delta\gamma$ are respectively the first-order variationals of J and γ; γ_{fa} is the adjoint variable of the filtered design variable γ_f. The term γ_{fa} in Eq. (5) is determined by sequentially solving the weak adjoint equations of the Young–Laplace equation and the Helmholtz filter:

$$\text{find } \bar{z}_a \in \mathcal{H}\left(\bar{\Omega}\right) \text{ with } \bar{z}_a = 0 \; at \; \bar{O}, \text{ satisfying:}$$

$$\int_{\bar{\Omega}} \frac{2}{\left|\bar{\Omega}\right|} \bar{z} \tilde{\bar{z}}_a - Bo^{-1} \frac{\nabla \bar{z}_a \cdot \nabla \tilde{\bar{z}}_a}{\sqrt{\left(L/z_0\right)^2 + \left|\nabla \bar{z}\right|^2}} + Bo^{-1} \frac{\left(\nabla \bar{z} \cdot \nabla \bar{z}_a\right) \left(\nabla \bar{z} \cdot \nabla \tilde{\bar{z}}_a\right)}{\left(\sqrt{\left(L/z_0\right)^2 + \left|\nabla \bar{z}\right|^2}\right)^3} \mathrm{d}\bar{\Omega} = 0, \; \forall \tilde{\bar{z}}_a \in \mathcal{H}\left(\bar{\Omega}\right), \tag{6}$$

$$\text{find } \gamma_{fa} \in \mathcal{H}\left(\bar{\Omega}\right) \text{ with } \gamma_{fa} = 0 \text{ at } \bar{O}, \text{ satisfying:}$$

$$\int_{\bar{\Omega}} -r_f^2 \nabla \gamma_{fa} \cdot \nabla \tilde{\gamma}_{fa} + \gamma_{fa} \tilde{\gamma}_{fa} - \frac{\partial Bo^{-1}}{\partial \gamma_p} \frac{\partial \gamma_p}{\partial \gamma_f} \frac{\nabla \bar{z} \cdot \nabla \bar{z}_a}{\sqrt{\left(L/z_0\right)^2 + \left|\nabla \bar{z}\right|^2}} \tilde{\gamma}_{fa} \, \mathrm{d}\bar{\Omega} = 0, \; \forall \tilde{\gamma}_{fa} \in \mathcal{H}\left(\bar{\Omega}\right), \tag{7}$$

where $\bar{z}_a$ and γ_{fa} are the adjoint variables of $\bar{z}$ and γ_f; $\tilde{\bar{z}}_a$ and $\tilde{\gamma}_{fa}$ are the test functions of $\bar{z}_a$ and γ_{fa}, respectively. The gradient of the duty ratio is determined by

$$\delta f_d = \int_{\bar{\Omega}} -\gamma_{fa} \delta\gamma \, \mathrm{d}\bar{\Omega}, \tag{8}$$

where δf_d is the first-order variational of the duty ratio f_d; γ_{fa} is derived by solving the weak adjoint equation of the Helmholtz filter:

$$\text{find } \gamma_{fa} \in \mathcal{H}\left(\bar{\Omega}\right) \text{ with } \gamma_{fa} = 0 \text{ at } \bar{O}, \text{ satisfying:}$$

$$\int_{\bar{\Omega}} -\frac{\partial \gamma_p}{\partial \gamma_f} \tilde{\gamma}_{fa} - r_f^2 \nabla \gamma_{fa} \cdot \nabla \tilde{\gamma}_{fa} + \gamma_{fa} \tilde{\gamma}_{fa} \, \mathrm{d}\bar{\Omega} = 0, \; \forall \tilde{\gamma}_{fa} \in \mathcal{H}\left(\bar{\Omega}\right). \tag{9}$$

The iterative procedure used for solving Eq. (4) is listed in Fig. 5. The finite element method is utilised to solve the relevant partial differential equations and corresponding adjoint equations, where a triangular element discretisation with maximal element size $1/240$ is used to discretise the dimensionless irreducible-triangles in Fig. 4. The finite element solution is implemented within the commercial softpackage *COMSOL Multiphysics* (www.comsol.com). The projection parameter β is doubled after every 30 iterations; the iterative loop is stopped when either the maximal iteration number is reached, or the averaged variation of the design objective in a run of 5 iterations and the residual of the duty-ratio constraint are simultaneously less than the specified tolerance 1×10^{-3}; the design variable is updated using the method of moving asymptotes [66].

3. Results and discussion

Based on the method introduced in Section 2, the micro-textures are investigated for the Cassie–Baxter mode of super-hydrophobicity. By solving the variational problem in Eq. (4) with the parameters listed in Table 1, the

```
Choose Bo_l, f_0, r_f and L;
Set i_max ← 315, i ← 1, γ ← f_0, β ← 1, ξ = 0.5, z_0 ← 1μm;
loop
    Filter and project the design variable;
    Evaluate the duty ratio of the micro-textures;
    Solve the dimensionless Young-Laplace equation;
    Evaluate the design objective and duty-ratio constraint;
    Solve the adjoint equations 6 and 7;
    Evaluate the adjoint derivative of the design objective;
    Solve the adjoint equation 9;
    Evaluate the adjoint derivative of the duty-ratio constraint;
    Update the design variable;
    if mod (i, 30) == 0
        β ← 2β;
    end(if)
    if i == i_max
        break;
    elseif β == 2^10, (1/5) Σ_{n=0}^{4} |J_i − J_{i−n}| / J_0 ≤ 10^−3 and |f_d − f_0| ≤ 10^−3;
        break;
    else
        continue;
    end(if)
    i ← i + 1
end(loop)
```

Fig. 5. Iterative procedure for solving the variational problem in Eq. (4), where i is the loop index, i_{max} is the maximal iteration number, and mod is the operator used to take the remainder.

Table 1
Parameters used for solving the variational problem in Eq. (4).

Bo_l	f_0	r_f	L
1	0.2	4/120	10 μm

micro-textures are derived for the three types of periodicity (Fig. 6), and they are generated by reflections, scalings, and extrusions of the physical density represented patterns in the dimensionless irreducible-triangles, demonstrated in Fig. 6. The derived micro-textures have quasi three-dimensional configurations, and they can be fabricated using a lithography-like process [67]. In the scaling-down operation, the scaling factor is the desired lattice constant; in the extruding operation, the extrusion height should be larger than the depth of the liquid/vapour interface, to avoid a collapse of the Cassie–Baxter mode caused by the liquid/vapour interface touching the bottom walls of the micro-textures, where the depth of the liquid/vapour interface can be calculated to be $\max_{\forall \mathbf{x} \in \bar{\Omega}} |z_0 \bar{z}|$. Fig. 6 shows that the trunks of the inversely designed patterns have ⋎, × and ⋇ topologies.

The convergence histories for the numerical calculation of the variational problems are plotted in Fig. 7; snapshots are included for the evolution of the physical density. From the monotonicity of the curves in Fig. 7, the robustness of the iterative procedure can be confirmed.

To demonstrate the optimality of the derived patterns, and hence the improved performance of the corresponding micro-textures, the normalised vertical coordinate distributions of the liquid/vapour interfaces supported by the micro-textures shown in Fig. 8a, c and e, are compared with the ones supported by corresponding regular polygonal-posts with the same duty ratio (Fig. 8b, d and f); the robustness-measurement values corresponding to the liquid/vapour interfaces shown in Fig. 8 are listed in Table 2. The comparison shows that the inversely designed micro-textures can achieve flatter liquid/vapour interfaces, and the computed robustness measurements are improved from 10^{-1} to 10^{-5}.

For the cells in Fig. 3, the quality of the inversely designed micro-textures are influenced by the Bond number, duty ratio, feature size and lattice constant. The effects of these factors are investigated as follows.

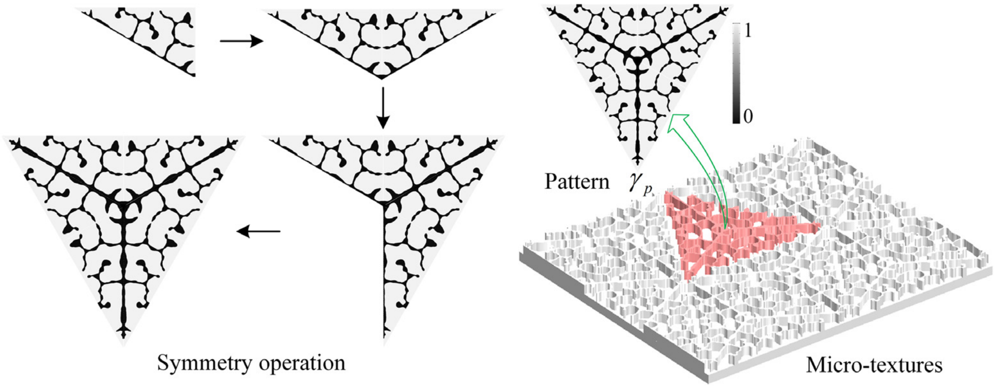

(a) Regular triangle

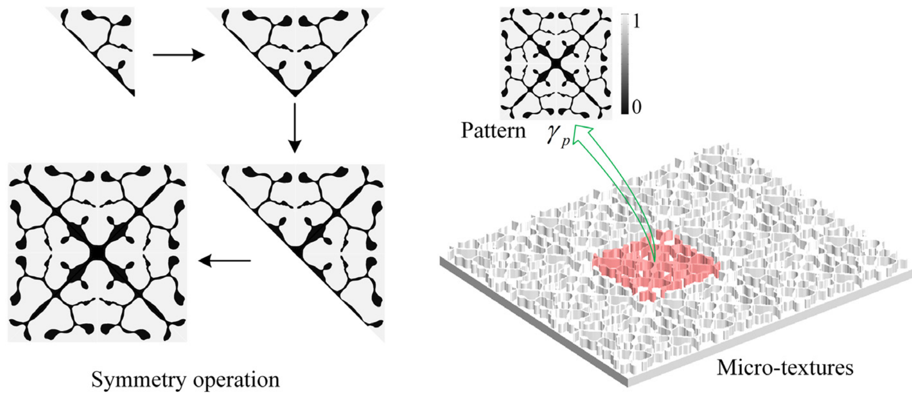

(b) Regular quadrangle

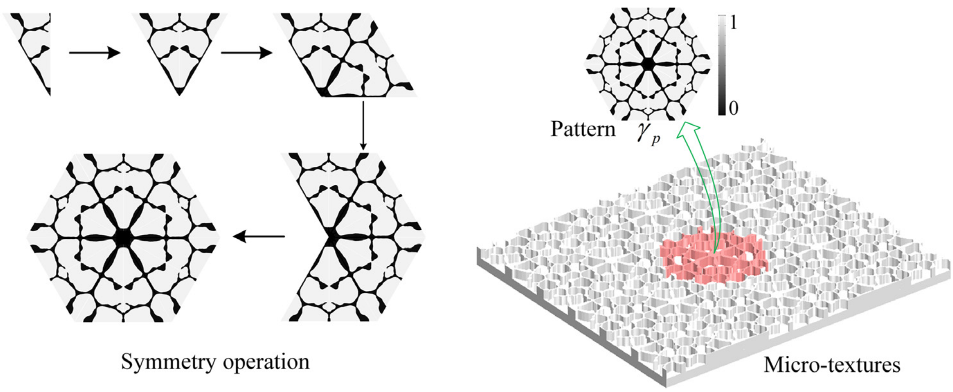

(c) Regular hexagon

Fig. 6. Inversely designed patterns for the three periodic micro-textures.

3.1. Effect of bond number

In Cassie–Baxter super-hydrophobicity, the convexity of the liquid/vapour interface strongly depends on the surface tension of the liquid and imposed physical pressure. To investigate this, micro-textures are inversely designed by choosing the Bond numbers $Bo_l \in \{1/5, 1/4, 1/3, 1/2, 1\}$; the other parameters are kept as listed in Table 1. The

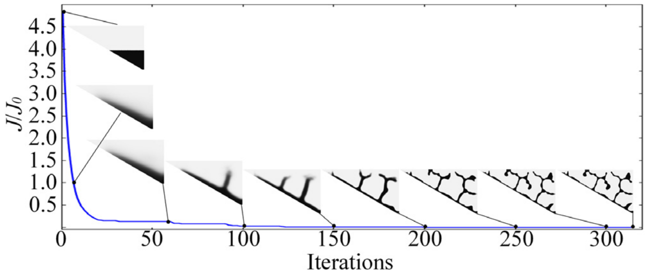

(a) Regular triangle

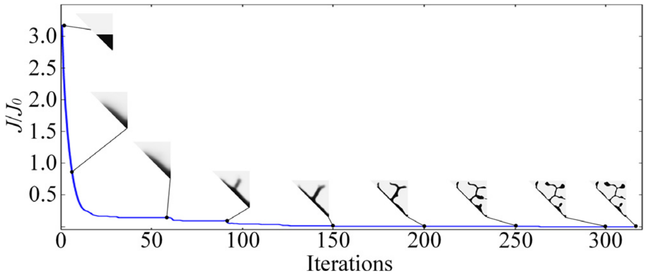

(b) Regular quadrangle

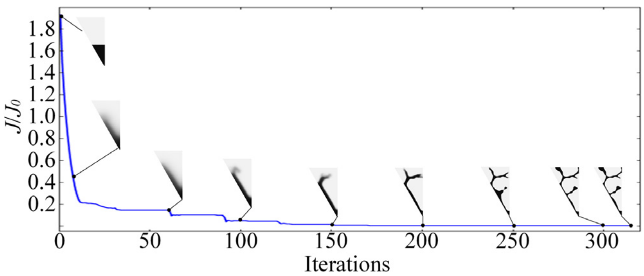

(c) Regular hexagon

Fig. 7. Convergent histories for the numerical calculation of the patterns in the dimensionless irreducible-triangles.

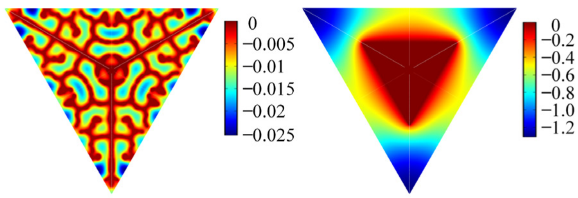

(a) (b)

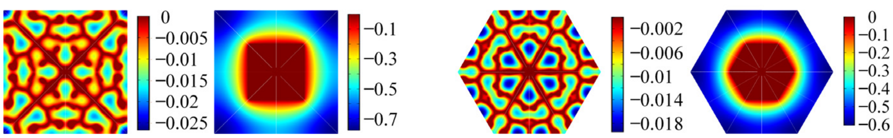

(c) (d) (e) (f)

Fig. 8. (a), (c) and (e) are the normalised vertical coordinate distributions of the liquid/vapour interfaces supported by the micro-textures corresponding to the patterns shown in Fig. 6. For comparison, the normalised vertical coordinate distributions are shown for the liquid/vapour interfaces respectively supported by the regular triangle, quadrangle and hexagonal posts with a duty ratio of 0.2, i.e., with the same amount of support material. The improvement in robustness is documented in Table 2.

Table 2
Robustness-measurement values corresponding to the liquid/vapour interfaces shown in Fig. 8.

(a) Regular triangle		(b) Regular quadrangle		(c) Regular hexagon	
	J		J		J
Fig. 8a	8.0388×10^{-5}	Fig. 8c	6.8213×10^{-5}	Fig. 8e	6.3817×10^{-5}
Fig. 8b	4.0530×10^{-1}	Fig. 8d	2.1711×10^{-1}	Fig. 8f	1.6897×10^{-1}

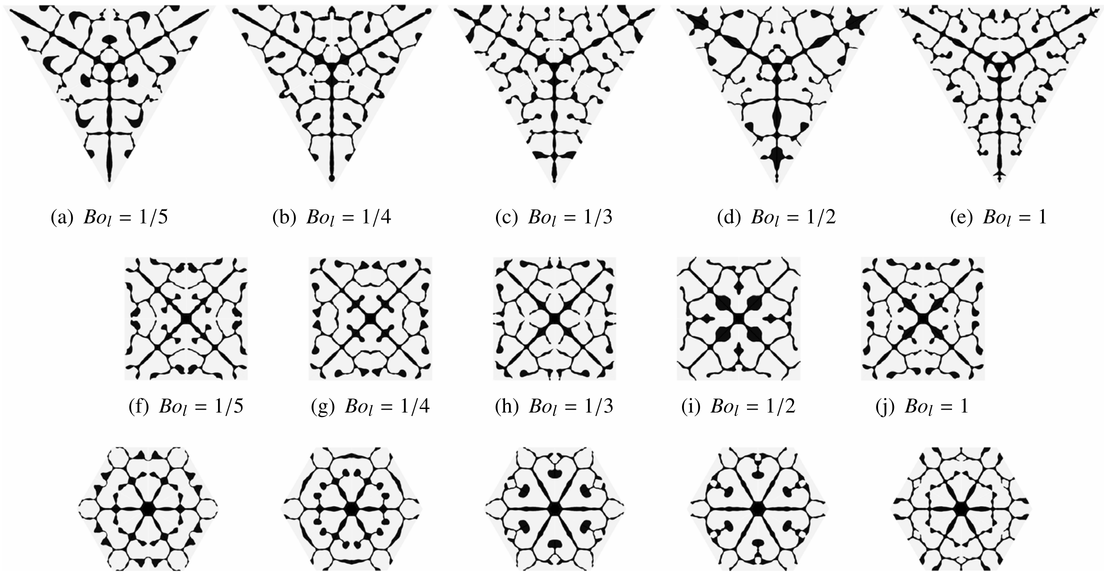

(a) $Bo_l = 1/5$ (b) $Bo_l = 1/4$ (c) $Bo_l = 1/3$ (d) $Bo_l = 1/2$ (e) $Bo_l = 1$

(f) $Bo_l = 1/5$ (g) $Bo_l = 1/4$ (h) $Bo_l = 1/3$ (i) $Bo_l = 1/2$ (j) $Bo_l = 1$

(k) $Bo_l = 1/5$ (l) $Bo_l = 1/4$ (m) $Bo_l = 1/3$ (n) $Bo_l = 1/2$ (o) $Bo_l = 1$

Fig. 9. Inversely designed patterns in the three regular lattices, for different Bond numbers; (a)–(e) for the periodicity with regular-triangle lattice, (f)–(j) for the periodicity with regular-quadrangle lattice, and (k)–(o) for the periodicity with regular-hexagon lattice.

derived patterns are shown in Fig. 9. The robustness-measurement values corresponding to the derived patterns are plotted in Fig. 10.

From Fig. 9, it can be concluded that the ⋎, × and ⋇ topologies are retained for the trunks of the inversely designed patterns. Under the same physical pressure, larger Bond numbers correspond to lower values of surface tension; hence, a liquid/vapour interface corresponding to a larger Bond number has a relatively weaker capability to sustain the liquid, and is prone to larger deformation for achieving larger curvatures to balance the pressure difference between the two sides of the interface. Therefore, the robustness-measurement values plotted in Fig. 10 increase nonlinearly along with an increase in Bond number.

To further conform the optimality of the inversely designed patterns, the robustness-measurement values corresponding to different Bond numbers are computed and listed in Table 3 for all the patterns in Fig. 9. From a cross comparison of the values in every column of the sub-tables, one can confirm the improvement of the micro-textures corresponding to the derived patterns.

3.2. Effect of duty ratio

For the periodic micro-textures, the apparent contact angle corresponding to the liquid/solid interface in the Cassie–Baxter mode can be calculated by $\cos\theta_C = -1 + f_0(\cos\theta + 1)$, where θ_C is the apparent contact angle on the structured surface and θ is the equilibrium contact angle on the underlying flat surface [53]. Therefore, for a surface with fixed hydrophobic-material, a smaller duty ratio of the micro-textures corresponds to larger apparent contact angle, under the precondition that the wetting behaviour is in the Cassie–Baxter mode. The specified duty ratios

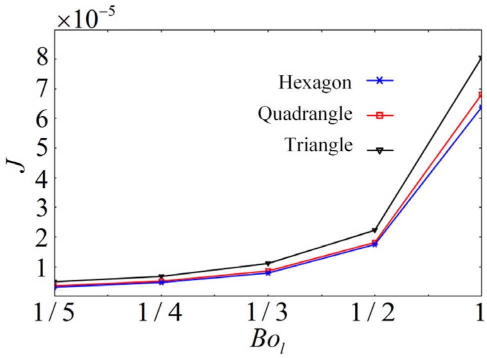

Fig. 10. Robustness-measurement values plotted for the inversely designed patterns shown in Fig. 9.

Table 3
Robustness-measurement values computed for the patterns derived in Fig. 9, for different Bond numbers. Note that the optimal entries for a given Bond number are noted in bold.

	$Bo_l = 1/5$	$Bo_l = 1/4$	$Bo_l = 1/3$	$Bo_l = 1/2$	$Bo_l = 1$
(a) Regular triangle					
Fig. 9a	$\mathbf{4.8184 \times 10^{-6}}$	1.0331×10^{-5}	1.6765×10^{-5}	3.4294×10^{-5}	1.2404×10^{-4}
Fig. 9b	5.9105×10^{-6}	$\mathbf{6.8462 \times 10^{-6}}$	1.3823×10^{-5}	2.8413×10^{-5}	1.0346×10^{-4}
Fig. 9c	5.4267×10^{-6}	7.7459×10^{-6}	$\mathbf{1.1028 \times 10^{-5}}$	2.5600×10^{-5}	9.2494×10^{-5}
Fig. 9d	8.4543×10^{-6}	1.2393×10^{-5}	2.0645×10^{-5}	$\mathbf{2.2392 \times 10^{-5}}$	1.6249×10^{-4}
Fig. 9e	7.2191×10^{-6}	8.4856×10^{-6}	1.2539×10^{-5}	4.3465×10^{-5}	$\mathbf{8.0388 \times 10^{-5}}$
(b) Regular quadrangle					
Fig. 9f	$\mathbf{3.5241 \times 10^{-6}}$	6.1475×10^{-6}	1.0225×10^{-5}	2.1480×10^{-5}	7.9985×10^{-5}
Fig. 9g	3.8976×10^{-6}	$\mathbf{5.1813 \times 10^{-6}}$	9.2993×10^{-6}	1.9317×10^{-5}	7.1084×10^{-5}
Fig. 9h	4.1979×10^{-6}	5.6506×10^{-6}	$\mathbf{8.6525 \times 10^{-6}}$	3.5523×10^{-5}	7.9601×10^{-5}
Fig. 9i	1.3515×10^{-4}	1.8248×10^{-5}	1.6569×10^{-5}	$\mathbf{9.7673 \times 10^{-6}}$	6.5432×10^{-6}
Fig. 9j	4.0846×10^{-6}	6.0132×10^{-6}	1.0057×10^{-5}	2.1246×10^{-5}	$\mathbf{6.8213 \times 10^{-5}}$
(c) Regular hexagon					
Fig. 9k	$\mathbf{3.1445 \times 10^{-6}}$	4.9730×10^{-6}	8.3960×10^{-6}	1.7909×10^{-5}	6.7708×10^{-5}
Fig. 9l	3.3471×10^{-6}	$\mathbf{4.6760 \times 10^{-6}}$	8.9365×10^{-6}	1.9191×10^{-5}	7.3118×10^{-5}
Fig. 9m	3.5174×10^{-6}	5.2590×10^{-6}	$\mathbf{7.9010 \times 10^{-6}}$	1.6866×10^{-5}	6.7054×10^{-5}
Fig. 9n	3.6211×10^{-6}	5.4047×10^{-6}	9.1680×10^{-6}	$\mathbf{1.7600 \times 10^{-5}}$	7.4765×10^{-5}
Fig. 9o	3.2105×10^{-6}	4.8083×10^{-6}	8.1837×10^{-6}	1.9654×10^{-5}	$\mathbf{6.3817 \times 10^{-5}}$

$f_0 \in \{0.1, 0.15, 0.2, 0.25, 0.3\}$ are investigated, with all other parameters listed in Table 1. After solving the variational problem in Eq. (4), the patterns are derived as shown in Fig. 11, and the corresponding robustness-measurement values are plotted in Fig. 12.

Fig. 11 shows that the $\curlyvee$, $\times$ and $\ast$ topologies are again maintained for the trunks of the inversely designed patterns for all lattices and duty ratios; however, the trunks become thicker and the branches around the trunks increase along with an increase in the duty ratio. For the patterns with low duty ratio, the micro-textures have a relatively weak capability to support the liquid/vapour interface. However, once the static pressure in the liquid is low enough, or the surface tension of the liquid is large enough, the stability of super-hydrophobicity can be enhanced towards a large apparent contact angle. On the other hand, the designer can improve the robustness of the Cassie–Baxter mode by specifying a relatively large duty ratio, because the inverse design procedure can ensure a minimal liquid-bulge volume held by the liquid/vapour interface. Because a lower duty ratio corresponds to larger deformation of the liquid/vapour interface, the robustness-measurement values decrease non-linearly along with the increase of the duty ratio, as plotted in Fig. 10.

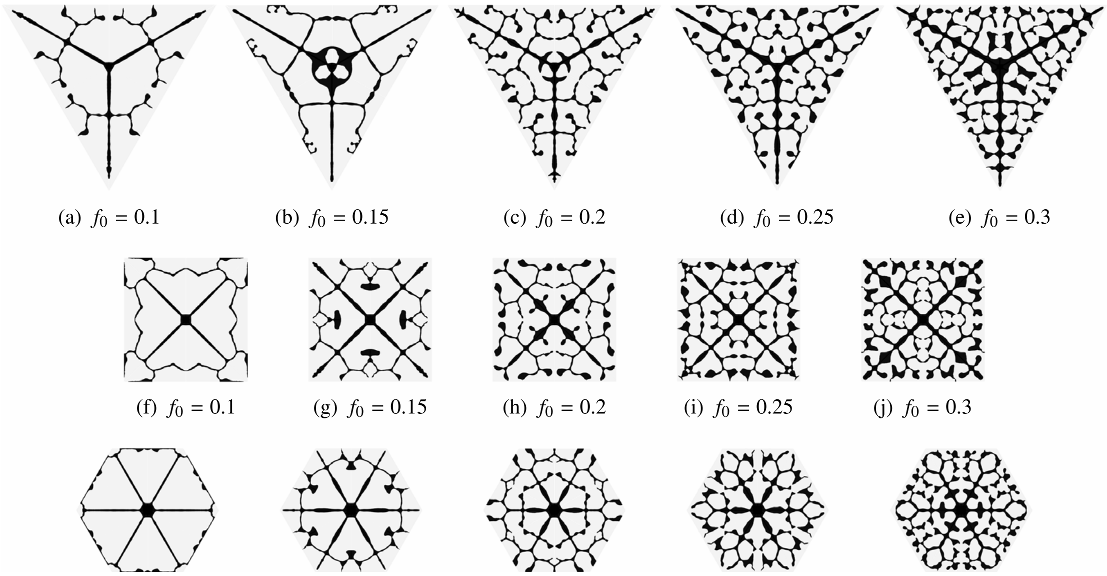

(a) $f_0 = 0.1$ (b) $f_0 = 0.15$ (c) $f_0 = 0.2$ (d) $f_0 = 0.25$ (e) $f_0 = 0.3$

(f) $f_0 = 0.1$ (g) $f_0 = 0.15$ (h) $f_0 = 0.2$ (i) $f_0 = 0.25$ (j) $f_0 = 0.3$

(k) $f_0 = 0.1$ (l) $f_0 = 0.15$ (m) $f_0 = 0.2$ (n) $f_0 = 0.25$ (o) $f_0 = 0.3$

Fig. 11. Inversely designed patterns in the three regular lattices, for different duty ratios; (a)–(e) for the periodicity with regular-triangle lattice, (f)–(j) for the periodicity with regular-quadrangle lattice, and (k)–(o) for the periodicity with regular-hexagon lattice.

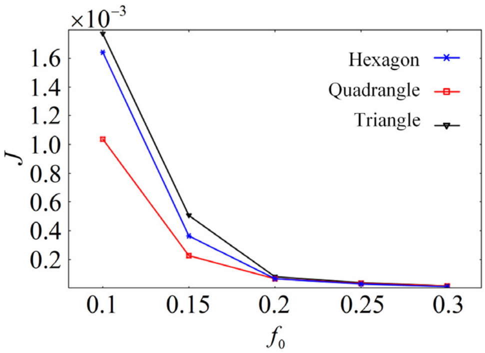

Fig. 12. Robustness-measurement values plotted for the inversely designed patterns shown in Fig. 11.

3.3. Effect of feature size

Manufacturability is one important evaluating factor for the quasi-3D micro-textures, and directly depends on the feature size of the derived pattern. Feature size is the smallest structure-size that can be tolerated by a fabrication process. The feature size of the pattern can be directly controlled by the radius of the Helmholtz filter in Eq. (4). The effect of the feature size is investigated by setting the filter radius respectively to be several different dimensionless values $r_f \in \{1/120, 2/120, 4/120, 8/120, 16/120\}$, and the other parameters as listed in Table 1. Corresponding to the filter radii, the patterns for the three dimensionless lattices are derived as shown in Fig. 13, and the corresponding robustness-measurement values are plotted in Fig. 14.

From the patterns derived in Fig. 13 and the robustness-measurement values plotted in Fig. 14, it can be concluded that the $\curlyvee$, $\times$ and $\ast$ topologies are similarly retained in the patterns with different feature sizes for all lattices; more branches of the patterns and more sophisticated morphology correspond to lower objective value and hence higher robustness of the Cassie–Baxter mode; when the filter radius is enlarged, the branches in the derived patterns become thicker, the number of branches are reduced, and the robustness of the Cassie–Baxter mode decreases exponentially

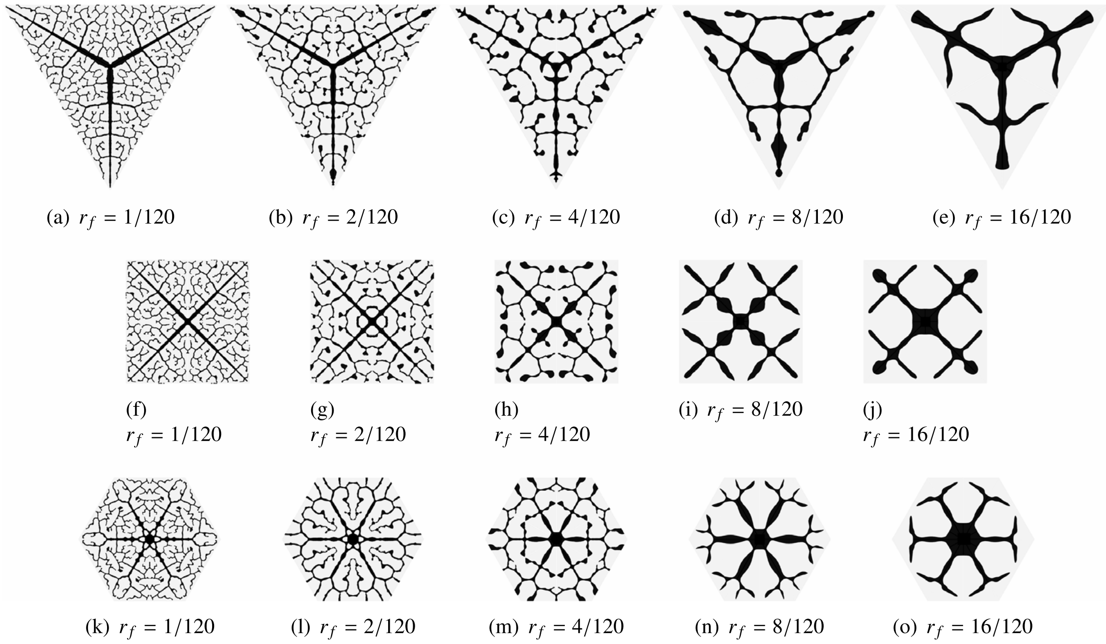

Fig. 13. Inversely designed patterns in the three regular lattices, for different feature sizes; (a)–(e) for the periodicity with regular-triangle lattice, (f)–(j) for the periodicity with regular-quadrangle lattice, and (k)–(o) for the periodicity with regular-hexagon lattice.

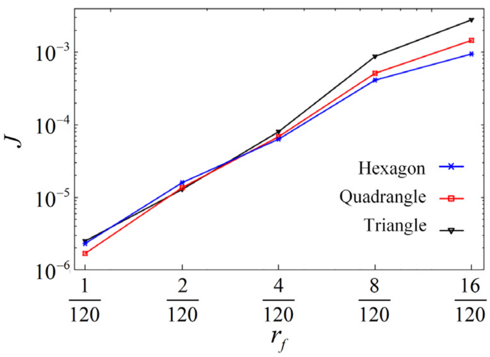

Fig. 14. Robustness-measurement values plotted for the inversely designed patterns shown in Fig. 13.

as a function of feature size. In practice, the designers can find a compromise between the manufacturability of the inversely designed micro-textures and the robustness of the Cassie–Baxter mode, by choosing a reasonable filter radius.

3.4. Effect of lattice constant

To investigate the effect of the lattice constant on the robustness of the Cassie–Baxter mode, patterns are inversely designed for the periodicity with lattice constants $L \in \{5, 10, 50, 100, 250, 500\}$ (μm), where the other parameters are kept as listed in Table 1. The patterns are derived as shown in Figs. 15–17. And the corresponding robustness-measurement values are plotted in Fig. 18.

In Figs. 15–17, both the topology and shape are exactly retained in the inversely designed patterns for all periodicity and across all chosen lattice constants. In Fig. 18, the robustness-measurement values increase with a power law as a function of the lattice constant; a smaller lattice constant corresponds to a flatter liquid/vapour interface and

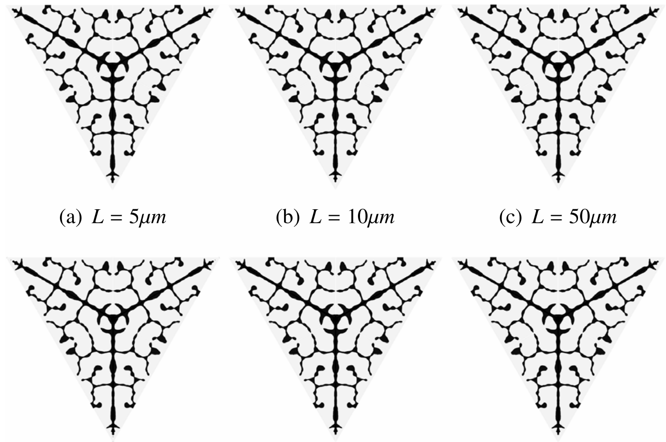

(a) $L = 5\mu m$ (b) $L = 10\mu m$ (c) $L = 50\mu m$

(d) $L = 100\mu m$ (e) $L = 250\mu m$ (f) $L = 500\mu m$

Fig. 15. Inversely designed patterns with different lattice constants in the regular-triangle lattices.

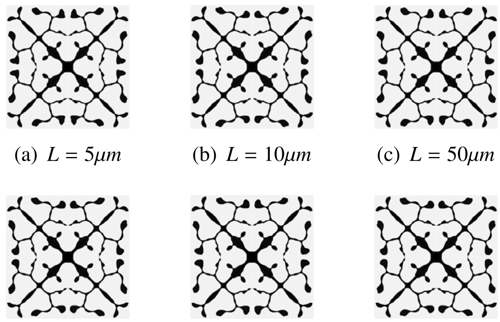

(a) $L = 5\mu m$ (b) $L = 10\mu m$ (c) $L = 50\mu m$

(d) $L = 100\mu m$ (e) $L = 250\mu m$ (f) $L = 500\mu m$

Fig. 16. Inversely designed patterns with different lattice constants in the regular-quadrangle lattices.

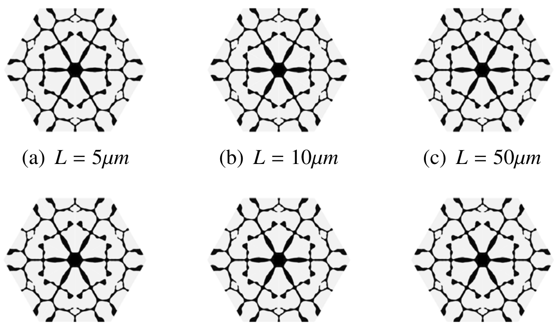

(a) $L = 5\mu m$ (b) $L = 10\mu m$ (c) $L = 50\mu m$

(d) $L = 100\mu m$ (e) $L = 250\mu m$ (f) $L = 500\mu m$

Fig. 17. Inversely designed patterns with different lattice constants in the regular-hexagon lattices.

more robust Cassie–Baxter mode. From Figs. 15–17, it is concluded that the inversely designed patterns can be scaled without losing their optimality in a reasonable lattice-constant range, in which the continuum hypothesis of the fluid (e.g. water) is ensured by mathematically describing the liquid/vapour interface to be a 2D manifold and

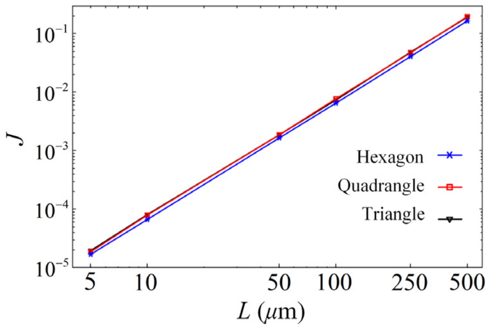

Fig. 18. Robustness-measurement values plotted for the inversely designed patterns shown in Figs. 15–17.

the dominant role of the surface tension guarantees the existence of the Cassie–Baxter mode for the corresponding wetting behaviour. This scaling property can be further confirmed by computing inversely designed patterns with other values of the Bond number, duty ratio, and feature size. The reason for the scaling property is that the solution of the Young–Laplace equation (1) can be scaled as:

$$z'\left(l_s\mathbf{x}\right) = l_s z\left(\mathbf{x}\right), \ \text{for } \forall\mathbf{x} \in \Omega, \ \forall l_s\mathbf{x} \in \Omega', \tag{10}$$

where l_s is the scaling factor; z' is the liquid/vapour interface on the scaled domain $\Omega' = \left\{\mathbf{x}' | \mathbf{x}' = l_s\mathbf{x}, \forall\mathbf{x} \in \Omega\right\}$. Based on the scaling property, it is favourable for the designer to compromise the robustness of the Cassie–Baxter mode and manufacturability of the corresponding micro-textures by choosing a reasonable lattice constant for the spacial periodicity.

The scaling property of inversely designed patterns also permits an approach to avoid that the elasto-capillary instability causes a collapse of the micro/nanostructures in the corresponding micro-textures. This instability has been widely observed [68–70]. In such phenomena, the capillary force decreases slowly, and this effect becomes dominant as the structure size is reduced [71]. Elastic micro/nanostructures can then be deformed by the common action of the capillary force and the liquid pressure, for periodic micro-textures with a small lattice constant. Based on reasonable scale-up of the inversely designed patterns and their cross-sectional aspect ratio, the pattern's stiffness can be enhanced; in this way, a collapse due to elasto-capillary interactions can be avoided.

Contact angle hysteresis is one important phenomenon of wetting of liquid droplets in micro-scales [56]. When the unit cell of the micro-textures is embedded periodically in an array, an increase in the equilibrium contact angle is accompanied by an attenuation effect for perturbations to the contact angle, where the solid surface is micro-textured by the unit-cell array with a fixed repeat size and the corresponding wetting behaviour is in the Cassie–Baxter state [17]. This attenuation effect increases along with the decrease in the ratio of the lattice constant L to repeat-array size L_r; and the micro-textured surface become "slippy", because the attenuation effect can weaken the contact angle hysteresis [17]. Therefore, the optimised micro-textures with relatively smaller length scale can weaken the contact angle hysteresis, where the wetting behaviour is in the Cassie–Baxter mode.

4. Conclusions

This paper has investigated the inversely-designed periodic micro-textures, with the goal to achieve the robust Cassie–Baxter mode of super-hydrophobicity, by the topology optimisation approach. The three different tiling periodicity of regular polygons that can fully cover a plane has been considered. The derived results reveal that the patterns always features with a trunk-like topology. And the trunk originates at the centre of the unit cell along the longest edge of the irreducible triangle, yielding the ultimate patterns with Y, × and ⚹ topologies.

We have studied the effects of the Bond number, duty ratio, feature size, and lattice constant on the formation of micro-textures. Based on a comparison of the derived patterns corresponding to different Bond numbers, the consistent optimality of the inverse design method has been confirmed. The effects of feature size and lattice constant have been shown to provide approaches for compromising the robustness of the Cassie–Baxter mode and manufacturability of the micro-textures. The effect of lattice constant permits scaling the derived patterns, and the scaling property provides an approach to avoid the collapse of micro/nanostructures caused by the elasto-capillary instability of structural deformation of the micro-textures.

From these studies, a monolithic inverse design procedure for the micro-textures on a solid surface can be proposed, by synthetically considering the manufacturability of the micro-textures, contact angle of the liquid, and surface-volume ratio of the liquid bulge:

1. Perform the inverse design of a pattern with specified duty ratio, feature size and lattice constant, for a liquid with known Bond number, where the lattice constant should be chosen to be small enough to ensure a dominant role of the surface tension.
2. Extract the geometry Ω_e corresponding to blankness of the derived pattern, and compute the liquid/vapour interface z supported by the micro-textures from the extracted geometry. A posteriori evaluation of the extracted geometry is implemented based on the following requirements: the maximal value of the contact angle at the boundary of the extracted geometry is not larger than its crucial advancing value at the side wall of the desired micro-textures, and the surface tension plays a dominant role, with the surface-to-volume ratio of the liquid bulge supported by the micro-textures being much larger than 1, i.e.

$$\begin{aligned} &\max_{\forall \mathbf{x} \in \partial \Omega_e} \theta(\mathbf{x}) \leq \theta_A, \\ &\frac{S_0}{V_0} \gg 1, \end{aligned} \tag{11}$$

where $\theta(\mathbf{x})$, demonstrated in Fig. 2, is the contact angle at the boundary of the extracted geometry; θ_A is the crucial advancing value of the contact angle, which can be determined from experimental measurements; S_0 and V_0 are the area and volume of the liquid bulge. The contact angle $\theta(\mathbf{x})$, area S_0, and volume V_0 can be calculated to be:

$$\begin{aligned} &\theta(\mathbf{x}) = \cos^{-1}\left(\frac{\nabla z}{|\nabla z|} \cdot \mathbf{n}_e\right), \ \forall \mathbf{x} \in \partial \Omega_e, \\ &S_0 = \int_{\Omega_e} \sqrt{1 + (\nabla z)^2}\, \mathrm{d}\Omega_e, \\ &V_0 = \left| \int_{\Omega_e} z \, \mathrm{d}\Omega_e \right|, \end{aligned} \tag{12}$$

where $\mathbf{n}_e$ is the unit normal vector at the boundary of the extracted geometry, pointing from the solid into the blankness. If the calculated contact angle and surface-volume ratio do not satisfy the relations in Eq. (11), the pattern should be re-designed by choosing a larger duty ratio or a smaller feature size; else, the extracted geometry can be retained for generating the periodic micro-textures.
3. Scale the extracted geometry using a reasonable scaling factor l_s, with maintaining the dominant role of the surface tension. Based on the scaling property in Eq. (10), the surface-volume ratio of the liquid bulge supported by the micro-textures, with the scaled and original geometries, satisfies

$$\frac{S_s}{V_s} = \frac{l_s^2 S_0}{l_s^3 V_0} = \frac{1}{l_s} \frac{S_0}{V_0} \gg 1, \tag{13}$$

where $S_s = l_s^2 S_0$ and $V_s = l_s^3 V_0$ are the area and volume of the liquid bulge supported by the micro-textures with the scaled geometry. Therefore, the chosen scaling factor should satisfy

$$l_s \ll \frac{S_0}{V_0}. \tag{14}$$

Under the precondition in Eq. (14), the extracted geometry is scaled up towards achieving improved manufacturability by choosing a scaling factor to be $l_s > 1$; else, it is scaled down to pursue a more robust Cassie–Baxter state.
4. Perform symmetry and extruding operations of the scaled geometry and establish the periodic micro-textures, whereby the extrusion distance should be larger than the depth of the supported liquid/vapour interface, i.e.

$$d_e > l_s \max_{\forall \mathbf{x} \in \Omega_e} |z|, \tag{15}$$

where d_e is the extrusion distance.

The derived micro-textures lend themselves to well-established micro and nano manufacturing processes, such as photo-polymer lithography, direct laser writing lithography, as well as nano-imprint lithography in order to achieve either a final surface or an initial tool geometry. Subsequent processing can be achieved for example by replication, such as hot embossing, soft lithography, or injection moulding.

Our design approach and the derived micro-textures can be used for applications requiring capillary-driven adsorption. The method can also be extended to inversely design micro-textures with dual scales or hierarchical configurations, including the consideration of the stiffness of the micro-structures, so as to further control the behaviour-stability. These topics will be investigated in our future work.

Acknowledgements

This work was supported by the Humboldt Research Fellowship for Experienced Researchers (Humboldt-ID: 1197305), the National Natural Science Foundation of China (Nos. 51405465, 61727813, 51605124, 51675506), the Youth Innovation Promotion Association of the Chinese Academy of Sciences (No. 2018253), and a Guest Professor Fellowship at the Karlsruhe Institute of Technology (KIT) via the DFG Metacoil project (KO 1883/20-1). During this project, J.G. Korvink was supported by an ERC Senior Grant (NMCEL, 290586) and by the Karlsruhe School of Optics and Photonics (KSOP). J.G. Korvink was also supported through the Cluster of Excellence BrainLinks-BrainTools (DFG, Grant No. EXC 1086). The authors are grateful to Prof. K. Svanberg for supplying the MMA codes. They are also grateful to the reviewers' kind attention and valuable suggestions.

References

[1] X. Feng, L. Jiang, Design and creation of superwetting/antiwetting surfaces, Adv. Mater. 18 (2006) 3063–3078.
[2] D. Öner, T.J. McCarthy, Langmuir 16 (2000) 7777.
[3] Q.J. Wang, Y.W. Chung, Encyclopedia of Tribology, Springer US, 2013.
[4] G. Jenkins, C.D. Mansfield, Microfluidic Diagnostics, Humana Press, 2013.
[5] J. Li, Y. Wei, Z. Huang, F. Wang, X. Yan, Z. Wu, Electrohydrodynamic behavior of water droplets on a horizontal super hydrophobic surface and its self-cleaning application, Appl. Surf. Sci. 403 (2017) 133–140.
[6] L. Feng, Z. Zhang, Z. Mai, Y. Ma, B. Liu, L. Jiang, D. Zhu, A super-hydrophobic and super-oleophilic coating mesh film for the separation of oil and water, Angew. Chem. Int. Ed. 43 (2004) 2012–2014.
[7] M. Kavalenka, F. Vllers, J. Kumberg, C. Zeiger, V. Trouillet, S. Stein, T. Ava, C. Li, M. Worgull, H. Hölscher, Adaptable bioinspired special wetting surface for multifunctional oil/water separation, Sci. Rep. (2017).
[8] P. Ragesh, V.A. Ganesh, S.V. Nair, A.S. Nair, A review on self-cleaning and multifunctional materials, J. Mater. Chem. A 2 (2014) 14773–14797.
[9] L. Feng, S.H. Li, Y.S. Li, H.J. Li, L.J. Zhang, J. Zhai, Y.L. Song, B.Q. Liu, L. Jiang, D.B. Zhu, Super-hydrophobic surfaces: from natural to artificial, Adv. Mater. 14 (2002) 1857.
[10] L. Feng, Y. Song, J. Zhai, B. Liu, J. Xu, L. Jiang, D. Zhu, Creation of a superhydrophobic surface from an amphiphilic polymer, Angew. Chem. Int. Ed. 42 (2003) 800–802.
[11] A.B. Gurav, Q. Guo, Y. Tao, T. Mei, Y. Wang, D. Wang, Durable, robust and free-standing superhydrophobic poly(vinyl alcohol-co-ethylene) nanofiber membrane, Mater. Lett. 182 (2016) 106–109.
[12] H. Yan, K. Kurogi, H. Mayama, K. Tsujii, Environmentally stable super water-repellent poly(alkylpyrrole) films, Angew. Chem. Int. Ed. 44 (2005) 3453.
[13] L. Jiang, Y. Zhao, J. Zhai, Angew. Chem. Int. Ed. 43 (2004) 4338.
[14] W. Wang, K. Lockwood, L.M. Boyd, M.D. Davidson, S. Movafaghi, H. Vahabi, S.R. Khetani, A.K. Kota, Superhydrophobic coatings with edible materials, ACS Appl. Mater. Interfaces 8 (29) (2016) 18664–18668.
[15] M. Reyssat, A. Pépin, F. Marty, Y. Chen, D. Quéré, Bouncing transitions on microtextured materials, Europhys. Lett. 74 (2006) 306–312.
[16] P. Ragesh, V.A. Ganesh, S.V. Nair, A.S. Nair, Condensation on ultrahydrophobic surfaces and its effect on droplet mobility: ultrahydrophobic surfaces are not always water repellant, Langmuir 22 (2006) 2433–2436.
[17] G. McHale, N.J. Shirtcliffe, M.I. Newton, Contact-angle hysteresis on super-hydrophobic surfaces, Langmuir 20 (2004) 10146–10149.
[18] W. Lee, M.K. Jin, W.C. Yoo, J.K. Lee, Nanostructuring of a polymeric substrate with well-defined nanometer-scale topography and tailored surface wettability, Langmuir 20 (2004) 7665–7669.
[19] C. Ukiwe, D.Y. Kwok, On the maximum spreading diameter of impacting droplets on well-prepared solid surfaces, Langmuir 21 (2005) 666–673.
[20] N.J. Shirtcliffe, G. McHale, M.I. Newton, G. Chabrol, C.C. Perry, Dual-scale roughness produces unusually water-repellent surfaces, Adv. Mater. 16 (2004) 1929–1932.
[21] L.R.J. Scarratt, B.S. Hoatson, E.S. Wood, B.S. Hawkett, C. Neto, Durable superhydrophobic surfaces via spontaneous wrinkling of Teflon AF, ACS Appl. Mater. Interfaces 8 (10) (2016) 6743–6750.
[22] W. Barthlott, C. Neinhuis, Planta 202 (1997) 1.
[23] X.F. Gao, L. Jiang, Nature 432 (2004) 36.

[24] F. Shi, Z. Wang, X. Zhang, Combinig a layer-by-layer assembling techinique with electrochemical deposition of gold aggregates to mimic the legs of water-striders, Adv. Mater. 17 (2005) 1005–1009.
[25] Z. Han, Z. Mu, W. Yin, W. Li, S. Niu, J. Zhang, L. Ren, Biomimetic multifunctional surfaces inspired from animals, Adv. Colloid Interface 234 (2016) 27–50.
[26] T. Sun, L. Feng, X. Gao, L. Jiang, Bioinspired surfaces with special wettability, Acc. Chem. Res. 38 (2005) 644–652.
[27] I. Ahmad, C. Kan, A review on development and applications of bio-inspired superhydrophobic textiles, Materials 9 (2016) 892.
[28] X. Yao, Y. Song, L. Jiang, Applications of bio-inspired special wettable surfaces, Adv. Mater. 23 (2011) 719–734.
[29] M. Liu, Y. Zheng, J. Zhai, L. Jiang, Bioinspired super-antiwetting interfaces with special liquid–solid adhesion, Acc. Chem. Res. 43 (2010) 368–377.
[30] S. Wang, K. Liu, X. Yao, L. Jiang, Bioinspired surfaces with superwettability: new insight on theory, design, and applications, Chem. Rev. 115 (2015) 8230–8293.
[31] M.P. Bendsoe, O. Sigmund, Topology Optimisation Theory, Methods and Applications, Springer, Berlin, 2003.
[32] B. Lazarov, O. Sigmund, Filters in topology optimisation based on Helmholtz type differential equations, Internat. J. Numer. Methods Engrg. 86 (2010) 765–781.
[33] T. Borrvall, J. Petersson, Topology optimisation of fluid in Stokes flow, Internat. J. Numer. Methods Fluids 41 (2003) 77–107.
[34] T. Nomura, K. Sato, K. Taguchi, T. Kashiwa, S. Nishiwaki, Structural topology optimisation for the design of broadband dielectric resonator antennas using the finite difference time domain technique, Internat. J. Numer. Methods Engrg. 71 (2007) 1261–1296.
[35] O. Sigmund, K.G. Hougaard, Geometric properties of optimal photonic crystals, Phys. Rev. Lett. 100 (2008) 153904.
[36] M.B. Duhring, J.S. Jensen, O. Sigmund, Acoustic design by topology optimisation, J. Sound Vib. 317 (2008) 557–575.
[37] W. Akl, A. El-Sabbagh, K. Al-Mitani, Topology optimisation of a plate coupled with acoustic cavity, Internat. J. Solids Struct. 46 (2008) 2060–2074.
[38] A. Gersborg-Hansen, M.P. Bendsoe, O. Sigmund, Topology optimisation of heat conduction problems using the finite volume method, Struct. Multidiscip. Optim. 31 (2006) 251–259.
[39] S. Zhou, W. Li, G. Sun, Q. Li, A level-set procedure for the design of electromagnetic metamaterials, Opt. Express 18 (2010) 6693–6702.
[40] S. Zhou, W. Li, Y. Chen, G. Sun, Q. Li, Topology optimisation for negative permeability metamaterials using level-set algorithm, Acta Mater. 59 (2011) 2624–2636.
[41] Y. Deng, J.G. Korvink, Self-consistent adjoint analysis for topology optimization of electromagnetic waves, J. Comput. Phys. 361 (2018) 353–376.
[42] Y. Deng, J.G. Korvink, Topology optimization for three-dimensional electromagnetic waves using an edge element-based finite-element method, Proc. R. Soc. Lond. Ser. A Math. Phys. Eng. Sci. 472 (2016) 20150835.
[43] M. Otomori, T. Yamada, K. Izui, S. Nishiwaki, J. Andkjær, A topology optimisation method based on the level set method for the design of negative permeability dielectric metamaterials, Comput. Methods Appl. Mech. Engrg. 237–240 (2012) 192–211.
[44] O. Sigmund, Materials with prescribed constitutive parameters: an inverse homogenisation problem, Internat. J. Solids Struct. 31 (1996) 2313–2329.
[45] Y. Deng, Z. Liu, P. Zhang, Y. Liu, Y. Wu, Topology optimisation of unsteady incompressible Navier–Stokes flows, J. Comput. Phys. 230 (2011) 6688–6708.
[46] Y. Deng, Z. Liu, J. Wu, Y. Wu, Topology optimisation of steady Navier–Stokes flow with body force, Comput. Methods Appl. Mech. Engrg. 255 (2013) 306–321.
[47] Y. Deng, Z. Liu, Y. Liu, Y. Wu, Combination of topology optimisation and optimal control method, J. Comput. Phys. 257 (2014) 374–399.
[48] O. Sigmund, K. Maute, Topology optimization approaches, Struct. Multidiscip. Optim. 48 (2013) 1031–1055.
[49] J.D. Deaton, R.V. Grandhi, A survey of structural and multidisciplinary continuum topology optimization: post 2000, Struct. Multidiscip. Optim. 49 (2014) 1–38.
[50] J.E. Cadman, S. Zhou, Y. Chen, Q. Li, On design of multi-functional microstructural materials, J. Mater. Sci. 48 (2013) 51–66.
[51] T. Young, An essay on the cohesion of fluids, Philos. Trans. R. Soc. Lond. 95 (1805) 65–87.
[52] R.N. Wenzel, Ind. Eng. Chem. 28 (1936) 988.
[53] A.B.D. Cassie, S. Baxter, Trans. Faraday Soc. 40 (1944) 546.
[54] J. Bico, C. Marzolin, D. Quéré, Europhys. Lett. 47 (1999) 220.
[55] A. Lafuma, D. Quéré, Nature Mater. 2 (2003) 457.
[56] H.B. Eral, D.J.C.M. 't Mannetje, J.M. Oh, Contact angle hysteresis: a review of fundamentals and applications, Colloid Polym. Sci. 291 (2013) 247–260.
[57] J. Toster, D. Lewis, Investigation of roughness periodicity on the hydrophobic properties of surfaces, Aust. J. Chem. 68 (2015) 1228–1232.
[58] T. Young, An essay on the cohesion of fluids, Phil. Trans. 65 (1805).
[59] P. Laplace, Supplement to the tenth edition. Méchanique céles 10, 1806.
[60] W.N. Bond, Nature 140 (3547) (1937) 716–716.
[61] K. Yosida, Functional Analysis, Springer, Berlin, 1980.
[62] B. Lazarov, O. Sigmund, Filters in topology optimisation based on Helmholtz type differential equations, Internat. J. Numer. Methods Engrg. 86 (2011) 765–781.
[63] F. Wang, B.S. Lazarov, O. Sigmund, On projection methods, convergence and robust formulations in topology optimisation, Struct. Multidiscip. Optim. 43 (2011) 767–784.
[64] J. Guest, J. Prevost, T. Belytschko, Achieving minimum length scale in topology optimisation using nodal design variables and projection functions, Internat. J. Numer. Methods Engrg. 61 (2004) 238–254.
[65] M. Hinze, R. Pinnau, M. Ulbrich, S. Ulbrich, Optimisation with PDE Constraints, Springer, Berlin, 2009.

[66] K. Svanberg, The method of moving asymptotes: a new method for structural optimisation, Internat. J. Numer. Methods Engrg. 24 (1987) 359–373.
[67] A. Pimpin, W. Srituravanich, Review on micro- and nanolithography techniques and their applications, Eng. J. 16 (2012) 37–55.
[68] C.V. Nguyen, L. Delzeit, A.M. Cassell, J. Li, J. Han, M. Meyyappan, Nano Lett. 2 (2002) 1079.
[69] K.K.S. Lau, J. Bico, K.B.K. Teo, M. Chhowalla, G.A.J. Amaratunga, W.I. Milne, G.H. McKinley, K.K. Gleason, Nano Lett. 3 (2003) 1701.
[70] D.H. Gracias, V. Kavthekar, J.C. Love, K.E. Paul, G.M. Whitesides, Adv. Mater. 14 (2002) 235.
[71] B. Roman, J. Bico, J. Phys.: Condens. Matter 22 (2010) 493101.